Journal of Mathematics in Industry
a SpringerOpen Journal

RESEARCH Open Access

A time-harmonic/time-domain hybrid approach based on displacement-based formulations to compute the absorbing coefficient in alpha cabins

Laura Río-Martín[1], Andrés Prieto[2*] and Alfredo Bermúdez[3]

*Correspondence:
andres.prieto@udc.es
[2]CITMAga, Departamento de Matemáticas, Universidade da Coruña, Campus Elviña, 15071, A Coruña, Spain
Full list of author information is available at the end of the article

Abstract

In the automotive industry, the absorption coefficient of a porous material layer is usually measured in an alpha cabin, a reverberant chamber of reduced dimensions where the operational frequency range is limited and the absorbent sample size is typically small. Those characteristics are well adapted to the requirements of automotive acoustics but far from the standard reverberant chambers used in building acoustics which ensures the conditions to perform measurements under a diffusive field. Since there are no standard norms to measure the absorption coefficient under non-diffusive fields, this work proposes a time-harmonic/time-domain hybrid approach to compute the absorption coefficient in alpha cabins. For this purpose, pointwise numerical predictions of the sound pressure level decay rate are used to calculate the absorption coefficient associated with a porous sample. To generate the pressure field acting inside the alpha cabin and, subsequently, approximate its decay rate, time-harmonic numerical simulations at a fixed frequency and a full time-dependent discretization of the wave problem have been considered. The proposed methodology is validated in a manufactured scenario where the exact solution is known in closed form. Finally, a realistic three-dimensional alpha cabin is deemed to predict the diffuse field absorption coefficient from the computed reverberation times using the proposed hybrid approach and the heuristic Sabine and Millington formulas.

Mathematics Subject Classification: 65M60; 65N30; 76N30

Keywords: Alpha cabin; Reverberation time; Absorbing coefficient; Finite element method

1 Introduction

In the automotive industry, the use of sound-absorbing or soundproofing materials is highly relevant not only for passengers' comfort purposes but also to mitigate long-term structural damage on sensible parts of the vehicles. The more widespread procedure to measure the absorption coefficient associated with a material layer is the Kundt tube, following the standard ISO 10534-2 [19]. This methodology allows us to compute the absorption coefficient of a porous sample at normal incidence. However, this coefficient does

not provide a complete overview of the mechanical behaviour of an absorbent trimmed component in its engineered location inside a vehicle because, in general, noise and vibrations are coming from very different directions rather than being focalized at normal incidence. Despite being possible to compute the absorption coefficient in diffuse field by using impedance tube data [24], the absorbent patches of porous materials used in the automotive industry are far from having planar surfaces, and they are not suitable for being used in a Kundt tube. Currently, the best-known experimental technique to evaluate the diffuse field absorption coefficient of a porous material layer consists of using a reverberation room [23, 28, 35, 36]. Concretely, in the automotive industry, the sound absorption coefficient of a porous material is often computed using the measurements coming from an alpha cabin [6], which typically is small-size in-house equipment (compared with the standard reverberation chambers used in building acoustics). Due to its reduced size, the accuracy of the experimental measurements has a limited low-pass frequency range, but it has the advantage of being well adapted to the requirements of porous trimmed components used in the automotive industry. Although the use of an alpha cabin is more affordable than other experimental facilities and requires smaller samples than a standard reverberation room, it involves two main challenges: the presence of diffraction effects due to the finite size of the porous material sample [11, 14], and the lack of diffusivity of the generated acoustic field inside the cabin, especially relevant at the low-frequency range where the absorbent components are less effective in the automotive vehicles [16].

Consequently, a numerical simulation approach becomes essential for evaluating the performance of a small-size alpha cabin and predicting the acoustic performance of porous samples of finite size at the low-frequency range. Instead of using classical methods such as ray methods [17] or image-source methods [12], this work presents a hybrid numerical approach where a finite element method is utilized to approximate the acoustic displacement field of a time-harmonic problem in the first stage and subsequently, a time-domain model is solved in a second stage. In the first stage, the (diffuse or not) acoustic field generated inside the alpha cabin is computed, whereas the second stage is focused on the prediction of the reverberation time of the acoustic field due to the presence of the porous sample.

Despite there are other numerical methods to compute reverberation times in interior acoustics, for instance, time-harmonic approaches entirely [3] (using inverse Fourier techniques to compute the impulse responses of the alpha cabin) or full time-domain methods [33] (using time-domain finite-difference discretizations), the proposed hybrid approach is the first novel attempt to combine both methods as far as the author's knowledge goes. This hybrid combination inherits the main computational advantages of time-harmonic and time-domain methods. More specifically, (a) the current hybrid approach is naively parallel to computing the frequency response of acoustic quantities of interest, such as the absorption coefficient; (b) the acoustic field generated at each frequency in the first stage of the hybrid approach eases the analysis of the diffusive character of the acoustic field in the alpha cabin, and hence quantify and identify frequency bands where the alpha cabin equipment can be used accurately; (c) the hybrid combination allows us to reduce the computational cost of the entire reverberation time computation since the time-marching scheme used in the second stage of the method has only to be applied to a reduced number of time steps. Hence, the proposed hybrid approach can efficiently predict the acoustic behaviour of in-house alpha cabin equipment even beyond the restrictive

dimensions imposed by the standards on reverberation rooms. The novelty of the present approach does not rely only on the computational advantages with respect to previous methodologies but also paves the way to developing new reduced-order model methods that take advantage of the displacement-based description of the spectral quadratic problem without the typical compact self-adjoint operators assumption.

The main goal of this work consists in a detailed description of the proposed hybrid approach to compute the frequency response at an arbitrary incident acoustic field associated with porous or fibrous samples installed in an alpha cabin. Section 2 describes the combination of time-harmonic and time-dependent problems to study the generation and decay behaviour of the acoustic field inside the cabin. More precisely, the time-harmonic source problem is written in terms of the displacement field, and its variational formulation and the finite element matrix formulation are discussed in detail. In Sect. 3, different approaches to computing the absorption values in a reverberation room are shown depending on ISO and ASTM standards, discussing the advantages and disadvantages of each one. Section 4 is devoted to performing simulations in two and three-dimensional domains. Section 4.1 considers a simple rectangular computational domain, where some manufactured experimental data have been used to validate the methodology under normal incident conditions. Then, a real-world fibrous material has been used to illustrate that it has been possible to obtain numerical results qualitatively similar to those reported by experimental data. Section 4.2 presents three-dimensional numerical simulations involving real fibrous sample data, and the computed absorption coefficient is compared with experimental data measured in a standard Kundt tube. Finally, Sect. 5 includes some remarks and conclusions about the obtained results and the proposed hybrid methodology.

2 Mathematical modelling

This section describes in detail the mathematical models and algorithmic procedure to compute the reverberation time in an alpha cabin with a hybrid time-harmonic/time-domain approach. For this purpose, the accurate approximation of the sound field inside the cabin is essential to calculating the absorption coefficient of porous samples installed on the interior surface of an alpha cabin. A displacement-based problem is used to describe the behaviour of the acoustic displacement field in an alpha cabin whose interior air occupies an arbitrary polyhedral computational domain Ω, which is supposed polyhedral. This domain has three disjoint boundaries, i.e., $\partial\Omega = \Gamma_L \cup \Gamma_I \cup \Gamma_N$, being Γ_L the boundary where the acoustic sources (loudspeakers) are placed, Γ_I the surface where the porous sample is located, and Γ_N are the rigid walls of the alpha cabin (see Fig. 1 for a schematic view of the alpha cabin).

Both standards ISO354:2003 and ASTM C423-09 involve a two-stage methodology to compute the reverberation time inside an alpha cabin. In the first step, the acoustic source located on Γ_L is turned on until the generated acoustic field reaches a time-harmonic state. Due to this reason, in order to simulate this step, it is necessary to solve a time-harmonic problem where a rigid wall boundary condition is imposed on Γ_N and an active acoustic source is prescribed on the surface Γ_L. Since the porous sample is modelled as a local reacting surface (see [15] for a detailed discussion on this assumption), a surface impedance condition is assumed on Γ_I, where the porous sample is located. Then, given a fixed angular frequency $\omega > 0$, the time-harmonic source problem of the first step in

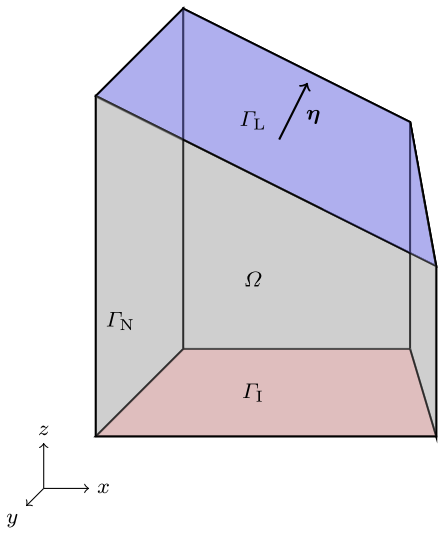

Figure 1 Schematic view of a three-dimensional polyhedral alpha cabin with an interior fluid cavity Ω, an active acoustic wall Γ_L (highlighted in blue), an absorbing sample Γ_I (highlighted in red), and rigid wall boundaries Γ_N (highlighted in gray). All the unit normal vectors $\boldsymbol{\eta}$ on its boundary $\partial\Omega$ are pointing outwards

the hybrid two-stage approach consists in finding the complex-valued displacement field $\boldsymbol{U}: \Omega \to \mathbb{C}^3$ such that

$$\begin{cases} -\rho_F c_F^2 \nabla(\operatorname{div} \boldsymbol{U}) - \omega^2 \rho_F \boldsymbol{U} = \boldsymbol{0} & \text{in } \Omega, \\ \boldsymbol{U} \cdot \boldsymbol{\eta} = 0 & \text{on } \Gamma_N, \\ -\rho_F c_F^2 \operatorname{div} \boldsymbol{U} = G & \text{on } \Gamma_L, \\ -\rho_F c_F^2 \operatorname{div} \boldsymbol{U} = (\alpha_s + i\omega\beta_s)\boldsymbol{U} \cdot \boldsymbol{m} & \text{on } \Gamma_I, \end{cases} \tag{1}$$

where ρ_F is the fluid mass density, c_F is the fluid sound speed, G is the acoustic pressure applied on the active surface of the loudspeakers, $Z_s(\omega) = \beta_s - i\alpha_s/\omega$ is the surface impedance associated with the sample involving the parameters $\alpha_s \geq 0$ and $\beta_s > 0$, and vectors $\boldsymbol{\eta}$ and $\boldsymbol{m}$ are the unit normal vectors to the interfaces Γ_N and Γ_I, respectively, pointing Ω inwards. From the time-harmonic assumption, the time-dependent displacement field is given by

$$\boldsymbol{u}(\boldsymbol{x}, t) = \operatorname{Re}(\boldsymbol{U}(\boldsymbol{x})e^{i\omega t}),$$

where recall that now $\boldsymbol{u}$ depends on the time variable t and the spatial position variable $\boldsymbol{x}$.

Remark 1 The local reacting assumption used to model the mechanical behaviour of the porous sample can be read as a simplification of much more sophisticated models, where both coefficients α_s and β_s depend on ω (see [10] for more realistic scenarios). However, in many cases for a narrow frequency band, the complex-valued surface impedance can be approximated by constants and hence, the parameters α_s and β_s are associated with the elastic and the viscous contribution of the walls (in analogy to the classical linear viscoelastic Kelvin-Voigt model [34]).

Once the time-harmonic state has been reached, the acoustic source is turned off, the sound pressure level will decrease, and the reverberation time is computed by measuring the decay rate at each angular frequency ω considered for the source problem (1). Hence, the second step in this hybrid approach requires the solution of a time-domain problem,

which governs the displacement field inside the alpha cabin without any acoustic source. To study the time evolution of the acoustic field once sources are turned off, it is necessary to solve the following time-dependent problem in the time interval $[0, T]$: find $u : \Omega \times [0, T] \to \mathbb{R}^3$ such that

$$\begin{cases} -\rho_{\mathrm{F}} c_{\mathrm{F}}^2 \nabla(\operatorname{div} \boldsymbol{u}) + \rho_{\mathrm{F}} \ddot{\boldsymbol{u}} = \boldsymbol{0} & \text{in } \Omega \times (0, T), \\ \boldsymbol{u} \cdot \boldsymbol{\eta} = 0 & \text{on } \Gamma_{\mathrm{N}} \times (0, T), \\ -\rho_{\mathrm{F}} c_{\mathrm{F}}^2 \operatorname{div} \boldsymbol{u} = 0 & \text{on } \Gamma_{\mathrm{L}} \times (0, T), \\ -\rho_{\mathrm{F}} c_{\mathrm{F}}^2 \operatorname{div} \boldsymbol{u} = \alpha_{\mathrm{s}} \boldsymbol{u} \cdot \boldsymbol{\eta} + \beta_{\mathrm{s}} \dot{\boldsymbol{u}} \cdot \boldsymbol{\eta} & \text{on } \Gamma_{\mathrm{I}} \times (0, T), \\ \boldsymbol{u}(\boldsymbol{x}, 0) = \boldsymbol{u}_0 & \text{in } \Omega, \\ \dot{\boldsymbol{u}}(\boldsymbol{x}, 0) = \boldsymbol{v}_0 & \text{in } \Omega, \end{cases} \tag{2}$$

where $\dot{\boldsymbol{u}} = \partial \boldsymbol{u}/\partial t$, $\ddot{\boldsymbol{u}} = \partial^2 \boldsymbol{u}/\partial t^2$, and $\boldsymbol{u}_0$ and $\boldsymbol{v}_0$ are the initial conditions for displacement and velocity (computed from the time-harmonic source problem (1)). More precisely, if $\boldsymbol{U}$ is the complex-valued displacement field solution of the time-harmonic source problem (1), then

$$\boldsymbol{u}_0(\boldsymbol{x}) = \operatorname{Re}(\boldsymbol{U}(\boldsymbol{x}) e^{i\omega t})|_{t=0} = \operatorname{Re}(\boldsymbol{U}(\boldsymbol{x})), \tag{3}$$

$$\boldsymbol{v}_0(\boldsymbol{x}) = \frac{\partial}{\partial t} \operatorname{Re}(\boldsymbol{U}(\boldsymbol{x}) e^{i\omega t})|_{t=0} = \operatorname{Re}(i\omega \boldsymbol{U}(\boldsymbol{x}) e^{i\omega t})|_{t=0} = \omega \operatorname{Im}(\boldsymbol{U}(\boldsymbol{x})). \tag{4}$$

In this manner, thanks to the use of these initial conditions defined from the solution of the time-harmonic source problem (1), both stages of the proposed computational approach are coupled. Obviously, other coupling values could be considered, using different initial conditions in terms of the imaginary part of the time-harmonic fields, or even taking into account any arbitrary linear combination of real and imaginary part. In any case, since only a constant complex-valued phase change would be introduced among the different choices of the initial conditions, the decay rates computed within the solution of the time-domain problem (2) would remain unaltered.

2.1 Variational formulation

Two different variational formulations must be derived for each stage of the proposed hybrid approach corresponding to the time-harmonic source problem (1) and the time-domain decay problem (2). Firstly, the time-harmonic source variational problem is described for a given fixed angular frequency $\omega > 0$ by the following statement: find $\boldsymbol{U} \in \mathbf{H}_{\Gamma_{\mathrm{N}}}(\operatorname{div}, \Omega; \mathbb{C})$ such that

$$\int_\Omega \rho_{\mathrm{F}} c_{\mathrm{F}}^2 \operatorname{div} \boldsymbol{U} \operatorname{div} \boldsymbol{W} \, \mathrm{d}V - \omega^2 \int_\Omega \rho_{\mathrm{F}} \boldsymbol{U} \cdot \boldsymbol{W} \, \mathrm{d}V + \int_{\Gamma_{\mathrm{I}}} \alpha_{\mathrm{s}} \boldsymbol{U} \cdot \boldsymbol{\eta} \boldsymbol{W} \cdot \boldsymbol{\eta} \, \mathrm{d}S + i\omega \int_{\Gamma_{\mathrm{I}}} \beta_{\mathrm{s}} \boldsymbol{U} \cdot \boldsymbol{\eta} \boldsymbol{W} \cdot \boldsymbol{\eta} \, \mathrm{d}S = -\int_{\Gamma_{\mathrm{L}}} G \boldsymbol{W} \cdot \boldsymbol{\eta} \, \mathrm{d}S, \tag{5}$$

for all $\boldsymbol{W} \in \mathbf{H}_{\Gamma_{\mathrm{N}}}(\operatorname{div}, \Omega; \mathbb{C})$, being

$$\mathbf{H}_{\Gamma_{\mathrm{N}}}(\operatorname{div}, \Omega; \mathbb{K}) = \left\{ \boldsymbol{W} : \Omega \to \mathbb{K}^3 : \boldsymbol{W} \in \left[\mathrm{L}^2(\Omega)\right]^3, \operatorname{div} \boldsymbol{W} \in \mathrm{L}^2(\Omega), \boldsymbol{W} \cdot \boldsymbol{\eta} \in \mathrm{L}^2(\partial\Omega), \boldsymbol{W} \cdot \boldsymbol{\eta} = 0 \text{ on } \Gamma_{\mathrm{N}} \right\}, \tag{6}$$

where $\mathbb{K} = \mathbb{C}$ is used for functional setting of the time-harmonic problem (5) and later $\mathbb{K} = \mathbb{R}$ for the time-dependent problem (7).

The analysis of uniqueness and existence of solution of the time-harmonic source problem (1) follows analogous arguments already used in [8]. The main difference with respect to the analysis made in [8] is the presence of a part of the boundary Γ_{L}, where a pressure value is prescribed. This fact requires the modification of the energy norm used in [8] to control the trace of the normal displacements of the solution (5) on that part of the boundary. Subsequently, some minor changes on the arguments to characterize the essential spectrum of the operators associated with its variational form.

In summary, the variational problem (5) is well-posed except for a countable sequence of complex-valued eigenfrequencies solution of a quadratic eigenvalue problem with an accumulation point at $i\alpha_{\mathrm{s}}/\beta_{\mathrm{s}}$. Notice also that, due to the presence of the porous sample in the alpha cabin, the eigenfrequencies associated with the alpha cabin have a strictly negative imaginary part, which implies an absorbing behaviour of the entire vibroacoustic system.

Remark 2 The displacement-based description of the time-harmonic vibroacoustic problem (1) has been chosen as an alternative to the classical pressure-based formulation due to the presence of the impedance boundary condition on Γ_{I}. In fact, the pressure-based formulation of the time-harmonic source problem (1) would lead to the following variational problem: find $P \in \mathrm{H}^1(\Omega)$ such that $P = G$ on Γ_{L} and

$$\int_{\Omega} \nabla P \cdot \nabla \bar{Q}\, \mathrm{d}V - \frac{\omega^2}{\alpha_{\mathrm{s}} + i\omega\beta_{\mathrm{s}}} \int_{\Gamma_{\mathrm{A}}} \rho_{\mathrm{F}} P \bar{Q}\, \mathrm{d}S - \frac{\omega^2}{c_{\mathrm{F}}^2} \int_{\Omega} P \bar{Q}\, \mathrm{d}V = 0 \qquad \forall Q \in \mathrm{H}^1_{\Gamma_{\mathrm{L}}}(\Omega),$$

with $\mathrm{H}^1_{\Gamma_{\mathrm{L}}}(\Omega) = \{Q \in \mathrm{H}^1(\Omega) :\ Q = 0 \text{ on } \Gamma_{\mathrm{L}}\}$. Obviously, the pressure-based spectral problem turns out to be neither linear nor quadratic [21]. Additionally, the use of a pressure-based formulation would require the initialization of the time-domain problem (2) with the time-derivative of the pressure field, which represents an uncommon physical quantity used in room acoustics, in comparison with the displacement and velocity fields used in the present approach.

Analogously, the weak formulation associated with the time-domain decay problem (2) can be stated using the time-dependent functional setting

$$\begin{aligned}
&\mathcal{C}^1([0,T], \mathbf{H}_{\Gamma_{\mathrm{N}}}(\mathrm{div}, \Omega; \mathbb{R})) \\
&\quad = \left\{ \boldsymbol{w} : \Omega \times (0,T) \to \mathbb{R}^3 : \boldsymbol{w}(\cdot,t), \dot{\boldsymbol{w}}(\cdot,t) \in \mathbf{H}_{\Gamma_{\mathrm{N}}}(\mathrm{div}, \Omega; \mathbb{R})\ \forall t \in [0,T] \right\}, \\
&\mathcal{C}^2((0,T), \left[\mathrm{L}^2(\Omega)\right]^3) \\
&\quad = \left\{ \boldsymbol{w} : \Omega \times (0,T) \to \mathbb{R}^3 : \boldsymbol{w}(\cdot,t), \dot{\boldsymbol{w}}(\cdot,t), \ddot{\boldsymbol{w}}(\cdot,t) \in \left[\mathrm{L}^2(\Omega)\right]^3\ \forall t \in (0,T) \right\},
\end{aligned}$$

and consequently, it is written as follows: Given $\boldsymbol{u}_0$ and $\boldsymbol{v}_0 \in \mathbf{H}_{\Gamma_{\mathrm{N}}}(\mathrm{div}, \Omega; \mathbb{R})$, find $\boldsymbol{u} \in \mathcal{C}^1([0,T], \mathbf{H}_{\Gamma_{\mathrm{N}}}(\mathrm{div}, \Omega; \mathbb{R})) \cap \mathcal{C}^2((0,T), \left[\mathrm{L}^2(\Omega)\right]^3)$, such that $\boldsymbol{u}(\cdot,0) = \boldsymbol{u}_0$, $\dot{\boldsymbol{u}}(\cdot,0) = \boldsymbol{v}_0$, and sat-

isfying

$$\int_\Omega \rho_F c_F^2 \operatorname{div} \boldsymbol{u} \operatorname{div} \boldsymbol{w} \, \mathrm{d}V + \int_\Omega \rho_F \ddot{\boldsymbol{u}} \cdot \boldsymbol{w} \, \mathrm{d}V + \int_{\Gamma_I} (\alpha_s \boldsymbol{u} \cdot \boldsymbol{\eta} + \beta_s \dot{\boldsymbol{u}} \cdot \boldsymbol{\eta}) \, \boldsymbol{w} \cdot \boldsymbol{\eta} \, \mathrm{d}S = 0, \tag{7}$$

for all $\boldsymbol{w} \in \mathcal{C}^1([0,T], \mathbf{H}_{\Gamma_N}(\mathrm{div}, \Omega; \mathbb{R}))$ in the time interval $(0,T)$.

The stability of the time-domain problem (7) follows directly by taking $\boldsymbol{w} = \boldsymbol{u}$. It is shown that the energy associated with the solution $\boldsymbol{u}$, given by

$$E(t) = \frac{1}{2}\left(\int_\Omega \rho_F c_F^2 |\operatorname{div} \boldsymbol{u}|^2 \, \mathrm{d}V + \int_\Omega \rho_F ||\dot{\boldsymbol{u}}||^2 \, \mathrm{d}V + \int_{\Gamma_I} \alpha_s |\boldsymbol{u} \cdot \boldsymbol{\eta}|^2 \, \mathrm{d}S \right),$$

decays as follows:

$$\frac{\mathrm{d}}{\mathrm{d}t} E(t) = -\int_{\Gamma_I} \beta_s |\dot{\boldsymbol{u}} \cdot \boldsymbol{\eta}|^2 \, \mathrm{d}S \leq 0. \tag{8}$$

This energy analysis in combination with the classical Hille-Yosida theory of time-evolution problems ensures the existence and uniqueness of the solution of the variational problem (7).

2.2 Spatial and time discretizations

The numerical approximation of the source and decay problems requires adequate spatial and time discretizations. For the time-harmonic source problem, a finite element method based on Raviart and Thomas elements [31] has been utilized. Thanks to the use of Raviart-Thomas finite elements no spurious curl modes has been observed in the numerical simulations performed in this study, which typically arise in this kind of displacement-based formulations (see [7, 22] for more details). The spatial discretization of the time-dependent problem could be chosen independently of the source time-harmonic problem. However, not only for simplicity but also to avoid interpolation errors to evaluate the approximations from one discrete finite element space to another different one, identical finite elements have been used on the same tridimensional simplicial mesh. In what follows, $\mathcal{T}_h$ denotes a quasi-uniform tetrahedral mesh of Ω, that is, $\Omega = \bigcup_{T \in \mathcal{T}_h} T$, which is conformal with the boundary partition described in Sect. 2 (each face of the elements of the mesh is contained uniquely either in Γ_I, Γ_L, or Γ_N).

2.2.1 Finite element discretization

To approximate the fluid displacements, $\boldsymbol{U} \in \mathbf{H}_{\Gamma_N}(\mathrm{div}, \Omega; \mathbb{K})$ with $\mathbb{K} = \mathbb{R}$ or $\mathbb{C}$, the lowest order Raviart-Thomas elements are used. These elements consist in vector valued functions such as, restricted to each tetrahedron, are incomplete linear polynomials of the form $\boldsymbol{U}_h(x_1, x_2, x_3) = (a + dx_1, b + dx_2, c + dx_3)$, $a, b, c, d \in \mathbb{K}$. Then the discrete Raviart-Thomas space is defined by

$$\mathbf{R}_h(\Omega; \mathbb{K}) = \{\boldsymbol{U}_h \in \mathbf{H}_{\Gamma_N}(\mathrm{div}, \Omega; \mathbb{K}) : \boldsymbol{U}_h|_T(x_1, x_2, x_3) = (a + dx_1, b + dx_2, c + dx_3), \\ a, b, c, d \in \mathbb{K}, \ \forall T \in \mathcal{T}_h\}. \tag{9}$$

These vector fields have constant normal components on each of the four faces of a tetrahedron (see Fig. 2), which define a unique polynomial function of this type. In particular,

Figure 2 Raviart-Thomas finite element. The degrees of freedom are the normal components of the vector unknown on the faces (normal vectors are highlighted in red)

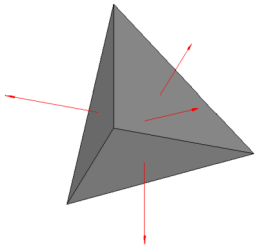

the lowest order of the Raviart-Thomas discrete functions $\boldsymbol{U}_h$ verify $\operatorname{div} \boldsymbol{U}_h$ is constant on each tetrahedron $T \in \mathcal{T}_h$, and, in fact, the divergence operator is surjective onto the space of piecewise constant functions defined on the mesh (see [9] for a detailed discussion). In addition, $\boldsymbol{U}_h \cdot \boldsymbol{\eta}|_{\partial T}$ is also constant on each face of the mesh, being $\boldsymbol{\eta}$ their unit normal vector. Due to this discrete feature, the number of degrees of freedom N_{dof} coincides with the number of faces of the mesh, and their values can be understood as the normal components of the discrete vector-valued function on the mesh faces.

By using this discrete Raviart-Thomas space, the function space $\mathbf{H}_{\Gamma_N}(\operatorname{div}, \Omega; \mathbb{K})$ can be replaced in the discrete problem by $\mathbf{R}_h(\Omega; \mathbb{K})$. In this manner, the discrete problem associated with the first step in the hybrid approach, i.e., the discretization of the time-harmonic variational formulation (5) is as follows: find $\boldsymbol{U}_h \in \mathbf{R}_h(\Omega; \mathbb{C})$ such that

$$\int_\Omega \rho_{\mathrm{F}} c_{\mathrm{F}}^2 \operatorname{div} \boldsymbol{U}_h \operatorname{div} \boldsymbol{W}_h \, \mathrm{d}V - \omega^2 \int_\Omega \rho_{\mathrm{F}} \boldsymbol{U}_h \cdot \boldsymbol{W}_h \, \mathrm{d}V + \int_{\Gamma_{\mathrm{I}}} \alpha_{\mathrm{s}} \boldsymbol{U}_h \cdot \boldsymbol{\eta} \boldsymbol{W}_h \cdot \boldsymbol{\eta} \, \mathrm{d}S + i\omega \int_{\Gamma_{\mathrm{I}}} \beta_{\mathrm{s}} \boldsymbol{U}_h \cdot \boldsymbol{\eta} \boldsymbol{W}_h \cdot \boldsymbol{\eta} \, \mathrm{d}S = -\int_{\Gamma_{\mathrm{L}}} G \boldsymbol{W}_h \cdot \boldsymbol{\eta} \, \mathrm{d}S, \quad (10)$$

for all $\boldsymbol{W}_h \in \mathbf{R}_h(\Omega; \mathbb{C})$. A matrix description can be introduced as it is usual in any linear problem discretized with a finite element method. Let $\vec{\boldsymbol{U}}_h$ be the column vector of coefficients of $\boldsymbol{U}_h$ in the basis $\{\boldsymbol{w}_j\}_{j=1}^{N_{\text{dof}}}$ associated to each degree of freedom in the discrete space $\mathbf{R}_h(\Omega; \mathbb{C})$,

$$\boldsymbol{U}_h(\boldsymbol{x}) = \sum_{j=1}^{N_{\text{dof}}} [\vec{\boldsymbol{U}}_h]_j \boldsymbol{w}_j(\boldsymbol{x}).$$

Then, the matrix formulation of the discrete problem (10) consists in finding $\vec{\boldsymbol{U}}_h \in \mathbb{C}^{N_{\text{dof}}}$ such that

$$-\omega^2 \mathbf{M} \vec{\boldsymbol{U}}_h + i\omega\beta_{\mathrm{s}} \mathbf{C} \vec{\boldsymbol{U}}_h + (\mathbf{K} + \alpha_{\mathrm{s}} \mathbf{C}) \vec{\boldsymbol{U}}_h = \vec{\boldsymbol{G}}_h,$$

where the coefficients of the mass, damping and stiffness matrices are, respectively,

$$[\mathbf{M}]_{ij} = \int_\Omega \rho_{\mathrm{F}} \boldsymbol{w}_j \cdot \boldsymbol{w}_i \, \mathrm{d}V,$$

$$[\mathbf{C}]_{ij} = \int_{\Gamma_{\mathrm{I}}} \boldsymbol{w}_j \cdot \boldsymbol{\eta} \boldsymbol{w}_i \cdot \boldsymbol{\eta} \, \mathrm{d}S,$$

$$[\mathbf{K}]_{ij} = \int_\Omega \rho_{\mathrm{F}} c_{\mathrm{F}}^2 \operatorname{div} \boldsymbol{w}_j \operatorname{div} \boldsymbol{w}_i \, \mathrm{d}V,$$

for $1 \leq i, j \leq N_{\text{dof}}$. The coefficients of the vector $\vec{\boldsymbol{G}}_h$ are the contributions of the source term to each degree of freedom $[\vec{\boldsymbol{G}}_h]_i = -\int_{\Gamma_L} G\boldsymbol{w}_i \cdot \boldsymbol{\eta}\, \mathrm{d}S$.

From a numerical algebra point of view, one of the most interesting numerical consequences of using displacement-based formulations in combination with finite element discretizations based on Raviart-Thomas elements is that matrix $\mathbf{C}$ is diagonal, and the bandwidth (number of non-null sub- and super-diagonals bandwidth) of matrices $\mathbf{M}$ and $\mathbf{K}$ is constant, independent of how the mesh $\mathcal{T}_h$ is refined. In particular, for the lowest order Raviart-Thomas elements, their bandwidth is seven (equal to the number of faces of two adjacent tetrahedra).

Similarly, the discretization of the time-dependent problem (7) can be defined as follows: given $\boldsymbol{u}_{0h}$ and $\boldsymbol{v}_{0h} \in \mathbf{R}_h(\Omega;\mathbb{R})$, find $\boldsymbol{u}_h \in \mathcal{C}^1([0,T],\mathbf{R}_h(\Omega;\mathbb{R})) \cap \mathcal{C}^2((0,T),\mathbf{R}_h(\Omega;\mathbb{R}))$, $\boldsymbol{u}_h(\cdot,0) = \boldsymbol{u}_{0h}$, $\dot{\boldsymbol{u}}_h(\cdot,0) = \boldsymbol{v}_{0h}$, and satisfying

$$\int_\Omega \rho_{\mathrm{F}} c_{\mathrm{F}}^2 \operatorname{div}\boldsymbol{u}_h \operatorname{div}\boldsymbol{w}_h \,\mathrm{d}V + \int_\Omega \rho_{\mathrm{F}} \ddot{\boldsymbol{u}}_h \cdot \boldsymbol{w}_h \,\mathrm{d}V + \int_{\Gamma_{\mathrm{I}}} \alpha_{\mathrm{s}} \boldsymbol{u}_h \cdot \boldsymbol{\eta}\boldsymbol{w}_h \cdot \boldsymbol{\eta}\,\mathrm{d}S + \int_{\Gamma_{\mathrm{I}}} \beta_{\mathrm{s}} \dot{\boldsymbol{u}}_h \cdot \boldsymbol{\eta}\boldsymbol{w}_h \cdot \boldsymbol{\eta}\,\mathrm{d}S = 0, \quad (11)$$

for all $\boldsymbol{w}_h \in \mathbf{R}_h(\Omega;\mathbb{R})$, and the initial data is given by $\boldsymbol{u}_{0h} = \mathrm{Re}(\boldsymbol{U}_h)$ and $\boldsymbol{v}_{0h} = \omega \mathrm{Im}(\boldsymbol{U}_h)$ due to the use of (3)-(4) in this discrete context. Consequently, the matrix description of the spatial discretization consists in an initial-value problem associated with a system of linear differential equations (involving first and second-order time derivatives) given by

$$\begin{cases} \mathbf{M}\dfrac{\mathrm{d}^2\vec{\boldsymbol{u}}_h}{\mathrm{d}t^2} + \mathbf{C}\dfrac{\mathrm{d}\vec{\boldsymbol{u}}_h}{\mathrm{d}t} + \mathbf{K}\vec{\boldsymbol{u}}_h = \mathbf{0} & \text{in } (0,T), \\ \vec{\boldsymbol{u}}_h(0) = \vec{\boldsymbol{u}}_{0h}, \\ \dfrac{\mathrm{d}\vec{\boldsymbol{u}}_h}{\mathrm{d}t}(0) = \vec{\boldsymbol{v}}_{0h}, \end{cases} \quad (12)$$

where the components of $\vec{\boldsymbol{u}}_h$ are the time-dependent coefficients used to represent $\boldsymbol{u}_h(\boldsymbol{x},t)$ as a linear combination of the Raviart-Thomas finite element basis, this is, $\boldsymbol{u}_h(\boldsymbol{x},t) = \sum_{j=1}^{N_{\text{dof}}} [\vec{\boldsymbol{u}}_h(t)]_j \boldsymbol{w}_j(\boldsymbol{x})$. If relations (3)-(4) between the time-harmonic discrete solution and the initial conditions of the time-dependent discrete problem are taken into account, thanks to the linearity of both problems, the initial data are given by $\vec{\boldsymbol{u}}_{0h} = \mathrm{Re}(\vec{\boldsymbol{U}}_h)$ and $\vec{\boldsymbol{v}}_{0h} = \omega \mathrm{Im}(\vec{\boldsymbol{U}}_h)$.

2.2.2 Time-marching scheme

Once a suitable finite element discretization has been introduced for the variational formulations stated above, a time-marching scheme must be chosen to discretize the time-dependent problem. A classical implicit Newmark scheme is used since this problem is second-order in time (acceleration $\ddot{\boldsymbol{u}}$ arises in the inertial term) [5]. This second-order scheme is unconditionally stable. Obviously, other implicit or explicit time-marching techniques could be used (see [29] for a detailed comparison). Taking into account this time-marching scheme, the displacement and velocity field are approximated by the following expressions:

$$\dot{\vec{\boldsymbol{u}}}_h^{n+1} = \dot{\vec{\boldsymbol{u}}}_h^{n} + [(1-\delta)\ddot{\vec{\boldsymbol{u}}}_h^{n} + \delta\ddot{\vec{\boldsymbol{u}}}_h^{n+1}]\Delta t, \quad (13)$$

$$\vec{\boldsymbol{u}}_h^{n+1} = \vec{\boldsymbol{u}}_h^n + \vec{\dot{\boldsymbol{u}}}_h^n \Delta t + [(1/2 - \alpha)\vec{\ddot{\boldsymbol{u}}}_h^n + \alpha \vec{\ddot{\boldsymbol{u}}}_h^{n+1}]\Delta t^2, \tag{14}$$

where $\Delta t = T/N_T$ is the time step, being N_T the number of time steps used in the entire numerical simulation, and α and δ are parameters that can be determined to obtain second-order accuracy and unconditional stability. Throughout the present work, $\alpha = 1/4$ and $\delta = 1/2$.

Solving from (14) $\vec{\ddot{\boldsymbol{u}}}_h^{n+1}$ in terms of $\vec{\boldsymbol{u}}_h^{n+1}$ and inserting this expression in (13), the following expression is obtained:

$$\vec{\dot{\boldsymbol{u}}}_h^{n+1} = \vec{\dot{\boldsymbol{u}}}_h^n + \Delta t(1-\delta)\vec{\ddot{\boldsymbol{u}}}_h^n + \Delta t \delta \vec{\ddot{\boldsymbol{u}}}_h^{n+1}. \tag{15}$$

By using the expressions (14) and (15), also the acceleration field $\vec{\ddot{\boldsymbol{u}}}_h^{n+1}$ can be computed in terms of the displacement field as follows:

$$\vec{\ddot{\boldsymbol{u}}}_h^{n+1} = \frac{1}{\alpha \Delta t^2}\left(\vec{\boldsymbol{u}}_h^{n+1} - \vec{\boldsymbol{u}}_h^n\right) - \frac{1}{\alpha \Delta t}\vec{\dot{\boldsymbol{u}}}_h^n - \left(\frac{1}{2\alpha} - 1\right)\vec{\ddot{\boldsymbol{u}}}_h^n. \tag{16}$$

Now, the expressions (15) and (16) can be substituted in the governing equation of the problem (12) at time t_{n+1} to obtain the following matrix formulation of the time-marching scheme:

$$\begin{aligned}\left(\frac{1}{\alpha \Delta t^2}\mathbf{M} + \frac{\delta}{\alpha \Delta t}\mathbf{C} + \mathbf{K}\right)\vec{\boldsymbol{u}}_h^{n+1} = \mathbf{M}\left(\frac{1}{\alpha \Delta t^2}\vec{\boldsymbol{u}}_h^n + \frac{1}{\alpha \Delta t}\vec{\dot{\boldsymbol{u}}}_h^n + \left(\frac{1}{2\alpha} - 1\right)\vec{\ddot{\boldsymbol{u}}}_h^n\right) \\ + \mathbf{C}\left(\frac{\delta}{\alpha \Delta t}\vec{\boldsymbol{u}}_h^n + \left(\frac{\delta}{\alpha} - 1\right)\vec{\dot{\boldsymbol{u}}}_h^n + \Delta t\left(\frac{\delta}{2\alpha} - 1\right)\vec{\ddot{\boldsymbol{u}}}_h^n\right),\end{aligned}$$

where $\vec{u}_h^{n+1}$ is computed at each time step t_{n+1} with $n = 0, \ldots, N_T$.

Remark 3 Despite a variety of implicit or explicit time-discretizations could have been used to solve the time-domain problem (2), the Newmark scheme with $\delta = 2\alpha = 1/2$ has been chosen to ensure that, even in those numerical simulations involving large time intervals or a weak absorption behaviour, the physical decay rate of the solution of the time-domain problem (2) is not polluted by the numerical dispersion introduced by the time-marching scheme.

Solving (2) by using the Newmark's scheme at each time $t_n = n\Delta t$, a sequence of approximated displacement fields $\vec{\boldsymbol{u}}_h^n$ are obtained for $n = 0, \ldots, N_T$. Associated with these displacement fields, it is straightforward to compute their respective approximations of the pressure field $p(\boldsymbol{x}, t)$ at different time steps, given by

$$p(\boldsymbol{x}, t_n) \approx p_h^n(\boldsymbol{x}) = -\rho_{\mathrm{F}} c_{\mathrm{F}}^2 \operatorname{div} \boldsymbol{u}_h(\boldsymbol{x}, t_n) = -\rho_{\mathrm{F}} c_{\mathrm{F}}^2 \sum_{j=1}^{N_{\mathrm{dof}}} [\vec{\boldsymbol{u}}_h^n]_j \operatorname{div} \boldsymbol{w}_j(\boldsymbol{x}) \qquad \text{for } n = 0, \ldots, N_T.$$

Again, due to the numerical properties of the Raviart-Thomas discretization, the post-processing computation of the pressure can be performed locally at each element of the mesh. In fact, for the lowest-order Raviart-Thomas finite element method, the discrete approximation of the pressure field is constant in each tetrahedron of the mesh.

Notice that other time-marching schemes could also be utilized to discretize the time-dependent problem. More precisely, the explicit Noh-Bathe second-order scheme (see [29] for further details) has also been used. Since the numerical results are similar to those obtained with the Newmark scheme, and the computational cost is slightly larger than the implicit scheme (since the Noh-Bathe requires a mild CFL stability condition), the numerical results obtained with that explicit time-marching scheme have not been included in this work.

3 Computation of the absorption values in an alpha cabin

Once the different mathematical models that govern the acoustic fields and the two-stage hybrid methodology have been explained in detail, and the time-harmonic and the time-dependent problems have been discretized, the absorption coefficient of a porous sample in an alpha cabin must be quantified. With this goal, the reverberation time associated with the porous sample in an alpha cabin is computed numerically. The international standards ASTM C423-09 [4] and ISO 354 (see [20] for more details) provide two different strategies to calculate the reverberation time. Additionally, different heuristic approximations can be used to compute the absorption coefficient from the reverberation time in the alpha cabin. This work follows the American standard ASTM to calculate the decay rates (computed using (20)) and the reverberation times associated with the alpha cabin. The main difference between ISO and ASTM standards relies on the fact that a strict application of the ISO norm requires the computation of the sound pressure level for a more extended time (until the sound pressure level has decreased by 60 dB). However, the use of the American standard involves the computation of the sound pressure level only over a reduced number of local time intervals. Hence, the ASTM procedure behaves locally while the ISO norm is based on an overall time methodology. For the sake of completeness, both standards are described in what follows.

3.1 Computation of the reverberation time using the ISO standard

Let $\{\boldsymbol{x}_m\}_{m=1}^{M}$ be a set of fixed spatial points used to measure the pressure field. The sound pressure level (SPL measured in decibels [dB]) at these points is given by

$$\mathrm{SPL}(t_n) = 20\log_{10}\left(\frac{1}{M}\sum_{m=1}^{M}\frac{|p_h^n(\boldsymbol{x}_m)|}{p_{\mathrm{ref}}}\right),$$

where $p_{\mathrm{ref}} = 2\times 10^{-5}$ Pa. Following the international norm ISO 354:2003 [20], the reverberation time of a closed room (in this case, an alpha cabin) is the time t_{rev} which satisfies

$$\mathrm{SPL}(t_{\mathrm{rev}}) = \mathrm{SPL}(0) - 60\ \mathrm{dB}, \tag{17}$$

i.e., the time (measured in seconds) required for the sound pressure level to decrease by 60 dB after turning off the acoustic source.

Typically, a different number of acoustic sources (loudspeakers) are included in the alpha cabin, and hence the procedure described above can be replicated independently for each acoustic source. Consequently, the reverberation time in the alpha cabin is obtained following the steps below, where it is assumed that each measurement can be performed independently for a fixed set of frequency values $\{\omega_l\}_{l=1}^{N_\omega}$:

(A) Repeat for each loudspeaker from $k = 1, \ldots, N_{\mathrm{L}}$: the k-th loudspeaker is turned on (exciting the alpha cabin at a fixed frequency value ω_l with $1 \leq l \leq N_\omega$), and $\mathrm{SPL}_{l,k}$ is obtained from the pressure values $p_{l,k}$ at the microphone locations $\{\boldsymbol{x}_m\}_{m=1}^{M}$ at discrete time steps $\{t_n\}_{n=0}^{N_T}$. Then, this loudspeaker is turned off.

(B) By using all the $\mathrm{SPL}_{n,k}$ for $k = 1, \ldots, L$ obtained in the previous step, the averaged SPL_n can be computed as follows:

$$\mathrm{SPL}_l(t_n) = \frac{1}{L}\sum_{k=1}^{N_{\mathrm{L}}} \mathrm{SPL}_{l,k}(t_n) = \frac{1}{L}\sum_{k=1}^{L}\left(20\log_{10}\left(\frac{1}{M}\sum_{m=1}^{M}\frac{|p_{l,k}(\boldsymbol{x}_m, t_n)|}{p_{\mathrm{ref}}}\right)\right), \tag{18}$$

where $p_{l,k}$ is the pressure field generated when the k-th loudspeaker is turned on (acting at a fixed frequency ω_l) and the rest is turned off.

(C) Finally, the reverberation time $t_{\mathrm{rev}}(\omega_l)$ is computed by solving (17), where $\mathrm{SPL}(t_{\mathrm{rev}}(\omega_l))$ has been calculated using the averaged SPL_l values (18).

Remark 4 The numerical results computed with this ISO methodology are far from accurate. In fact, very low absorption values are obtained, which are not comparable with the actual values of the porous sample. The origin of this lack of accuracy in the numerical results has been identified, and it is related to the pointwise computation of $SPL_{l,k}$ values associated with the numerical evaluation of the pressure field at a particular time value. Those values computed at specified time steps are prone to contain spurious oscillations due to numerical pollution or dispersion errors, which leads to unrealistic reverberation time values.

3.2 Computation of decay rates using the ASTM standard

A different local average-based and more robust strategy can be designed to avoid all the above-mentioned drawbacks in the ISO standard. More precisely, the ASTM standard uses decay rates on time windows of a reduced length instead of pressure values at concrete times. Once the time-dependent problem (11) has been solved and subsequently, the pressure field p_l post-processed at each discretization time step $t_n = n\Delta t$ for $n = 0, \ldots, N_T$ from an initial data generated with all the loudspeakers turned on acting at a given frequency ω_l with $l = 1, \ldots, N_\omega$, the ASTM standard [4] proposes to compute local averages of the sound pressure level in time windows of length δt. The (j,l)-th local average of the sound pressure level $L_{\mathrm{eq},j,l}$ (see Equation (1) in [2]) is computed as follows:

$$L_{\mathrm{eq},j,l} = \frac{1}{M}\sum_{m=1}^{M} 10\log_{10}\frac{1}{\delta t}\int_{(j-1)\delta t}^{j\delta t}\frac{|p_l(\boldsymbol{x}_m, t)|^2}{p_{\mathrm{ref}}^2}\mathrm{d}t, \tag{19}$$

for $j = 1, \ldots, D$ and $l = 1, \ldots, N_\omega$, being D the number of computed local averages. From a numerical point of view, the integral in (19) has been approximated by a composite Simpson's rule using the discrete pressure values $p_h^n(\boldsymbol{x}_m)$ with $t_n \in [(j-1)\delta t, j\delta t]$, prescribing that $\delta t/\Delta t$ is an integer.

As the ASTM standard recommends (see Equation (5) in [4]), the decay rate is the absolute value of the slope of the linear regression model $\hat{L}_{\mathrm{eq},l,j} = -d_{\mathrm{rev},l}(j\delta t) + b_l$ computed with the average sound pressure level dataset $\{(j\delta t, L_{\mathrm{eq},j,l})\}_{j=1}^{D}$. This slope is computed by

using the following expression:

$$d_{\mathrm{rev},l} = -\frac{D\sum_{j=1}^{D}(j\delta t)L_{\mathrm{eq},j,l} - \left(\sum_{j=1}^{D} j\delta t\right)\left(\sum_{j=1}^{D} L_{\mathrm{eq},j,l}\right)}{D\sum_{j=1}^{D}(j\delta t)^2 - \left(\sum_{j=1}^{D} j\delta t\right)^2}$$
$$= \frac{6}{D(D^2-1)\delta t}\left[(D+1)\sum_{j=1}^{D} L_{\mathrm{eq},j,l} - 2\sum_{j=1}^{D} jL_{\mathrm{eq},j,l}\right]. \tag{20}$$

Once the decay rate associated with each frequency is computed, the reverberation time can be computed as $t_{\mathrm{rev}}(\omega_l) = 60/d_{\mathrm{rev},l}$ for $l = 1,\ldots,N_\omega$.

Obviously, other possible numerical procedures based on time averages can be applied to estimate the decay rate associated with the time evolution of the pressure field in an alpha cabin. In particular, the two additional time-average algorithms are also analyzed, which use

SPL regression: the slope of the linear regression response of the sound pressure level computed from the pressure values at all time steps $t_n = n\Delta t$ with $n = 0\ldots,N_T$ (without using the local averages described above),

L_2*-norm regression*: the slope of the linear regression response of the root-mean-square of the pressure values in the entire alpha cabin at all time steps $t_n = n\Delta t$ with $n = 0\ldots,N_T$ given by

$$\mathrm{L}_2\text{-norm}\left[p_l\right](t_n) = \frac{1}{L}\sum_{k=1}^{L}\sqrt{\int_\Omega |p_{l,k}(\boldsymbol{x},t_n)|^2\,\mathrm{d}V},$$

where it has not been taken into account the pointwise pressure values at the microphone locations. The associated SPL values to this root-mean-square pressure values are computed coherently with (18) by $20\log_{10}(\mathrm{L}_2\text{-norm}\left[p_l/p_{\mathrm{ref}}\right](t_n))$ with $n = 0\ldots,N_T$.

Throughout the rest of this work, these two strategies together with the ISO and ASTM procedures described above, have been analyzed in terms of the numerical results.

3.3 Heuristic computation of the absorption coefficient

Once the computation of the reverberation time in an alpha cabin has been described in detail, the absorption coefficient of a porous sample installed in the alpha cabin should be estimated. Following the American standard ASTM C423-09 [4] or the international norm ISO 354:2003 [20], the heuristic Sabine and Millington formulas can be utilized.

From Sabine formula [32], the absorption coefficient $\alpha(\omega)$ of the sample is given by

$$\alpha(\omega) = \frac{6\ln(10)L}{c_{\mathrm{F}}}\left(\frac{1}{t_{\mathrm{rev}}(\omega)} - \frac{1}{t_{\mathrm{empty}}}\right), \tag{21}$$

where c_{F} is the air sound speed, L is the typical length of the cabin (distance travelled by a ray between two consecutive wall reflections), and $t_{\mathrm{rev}}(\omega)$ and t_{empty} are the reverberation

time with and without the porous sample in the alpha cabin. The typical length of the cabin is given by

$$L = \begin{cases} V/S & \text{at normal incidence,} \\ 4V/S & \text{at diffuse field,} \end{cases} \tag{22}$$

where V is the total volume of the alpha cabin and S is the surface occupied by the absorbing test specimen. Notice that the floor of the alpha cabin is assumed to be rigid.

Alternatively, instead of computing the absorption coefficient using the simpler Sabine formula, $\alpha(\omega)$ can be computed with the classical Millington formula [26], which is more robust for absorption values close to zero (see [13] for more details)

$$\ln(1-\alpha(\omega)) = \frac{6\ln(10)L}{c_{\mathrm{F}}}\left(\frac{1}{t_{\mathrm{rev}}(\omega)} - \frac{1}{t_{\mathrm{empty}}}\right). \tag{23}$$

Since the boundary of the alpha cabin is considered rigid in (2), when the porous sample is removed (the alpha cabin is empty), (8) shows there is no energy decay. Consequently, the reverberation time associated with the alpha cabin can be considered infinite, and the term $1/t_{\mathrm{empty}}$ is neglected in both expressions (21) and (23).

4 Numerical results

In this section, some numerical results illustrate the time-harmonic/time-domain hybrid methodology to compute the reverberation times and, subsequently, to estimate the absorption coefficient of a porous sample in an alpha cabin. Some two-dimensional simulations are performed to validate the proposed approach. Additionally, a realistic three-dimensional geometry of an alpha cabin is considered to compare the numerical results to experimental measurements in a Kundt's tube.

4.1 Two-dimensional numerical simulations

First of all, some two-dimensional simulations are performed. This section includes the description of the used geometry and the numerical results with two different datasets: manufactured data to validate the proposed approach and experimental data of an engineered fibrous material. In both cases, $\Omega = (0,1)\times(0,0.75)$ and its boundary is split into an absorbing wall Γ_{I}, a piston-like wall Γ_{L} where the acoustic source is located, and rigid walls Γ_{N}. There are six microphones located within Ω at the positions $\boldsymbol{x}_m = (0.1(1+m), 0.1)$ with $m = 1,\ldots,M = 6$. A schematic view of this computational domain is shown in Fig. 3.

4.1.1 Validation test with manufactured data

First, the implementation of the proposed hybrid approach has been validated using manufactured data for the porous sample, which consists in the frequency response of the absorption coefficient at diffuse field. The time-harmonic problem (1) and the time-dependent problem (2) have been solved to compute the absorbing coefficient using the time-harmonic/time-domain hybrid methodology. Thanks to the approximation of the pressure field inside the alpha cabin, the reverberation time can be computed and finally, the absorption coefficient of the material is obtained. In this case, it has been assumed that the porous sample has a surface impedance smaller than the characteristic impedance of the surrounding air. More precisely, it is chosen $Z(\omega) = \beta_{\mathrm{s}} - i\alpha_{\mathrm{s}}/\omega$ with $\alpha_{\mathrm{s}} = 0$ Ns/m^3 and

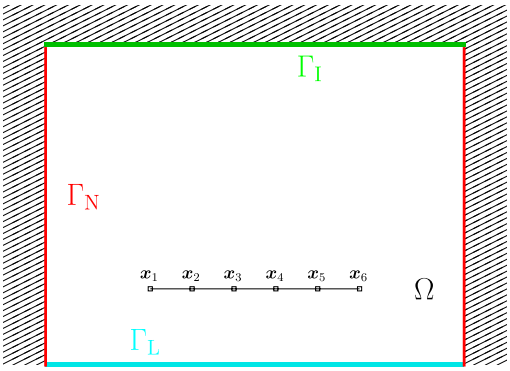

Figure 3 Two-dimensional computational domain $\Omega = (0,1) \times (0,0.75)$, whose boundary is split into an absorbing wall Γ_I (highlighted in green), one piston-like wall Γ_L (highlighted in cyan), and two rigid walls Γ_N (highlighted in red). The six microphones are located at points $\boldsymbol{x}_1, \ldots, \boldsymbol{x}_6$

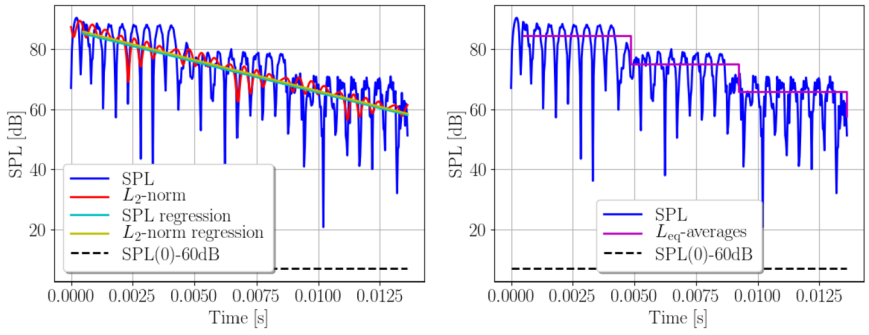

Figure 4 Time evolution of the sound pressure level generated at 1000 Hz in an alpha cabin with an installed porous sample, whose surface impedance is $Z(\omega) = \beta_s - i\alpha_s/\omega$, with $\alpha_s = 0$ Ns/m^3 and $\beta_s = 206.21$ Ns/m^3. Left: values of the SPL computed using (18) (blue line), and those obtained by using the L2-norm of the pressure field (red line), regression line calculated globally by using the SPL data at every time step (cyan line), and regression line computed globally by utilizing the L_2-norm of the pressure field (yellow line). Right: values of the SPL calculated by using (18)(blue line) and regression lines obtained from the local L_{eq}-averages obtained from (19), where the time-window length is $\delta t = 0.00439$ s (magenta line). The dashed black line in both plots represents the SPL value where the initial sound pressure level has decreased by 60 dB

$\beta_s = 206.21$ Ns/m^3. The absorbing coefficient is computed in a frequency range from 400 to 1000 Hz in third-octave bands (400, 500, 630, 800, and 1000 Hz).

Once the pressure field is evaluated at the microphone locations, the sound pressure level can be computed at each angular frequency. The four strategies described in Sect. 3 have been utilized to calculate the reverberation time: (i) the SPL criterion of the ISO standard, (ii) the local L_{eq}-averages of the ASTM standard, (iii) the overall SPL regression using the time response of the SPL at the microphone locations, and (iv) the L_2-norm regression using the root-mean-square of the pressure field in the entire alpha cabin.

The right plot in Fig. 4 shows that only four values of the local L_{eq}-averages have been computed in the ASTM standard, since the time window length has been settled to $\delta t = 0.00439$ s, and the final time is $T = 0.014$ s. Obviously, in the left plot in Fig. 4, a more extended time interval would be necessary to reach a time step where the initial SPL value decreases by 60 dB, which would lead to an unnecessary increase in the computational cost of solving the time-dependent problem (2). As discussed above, the

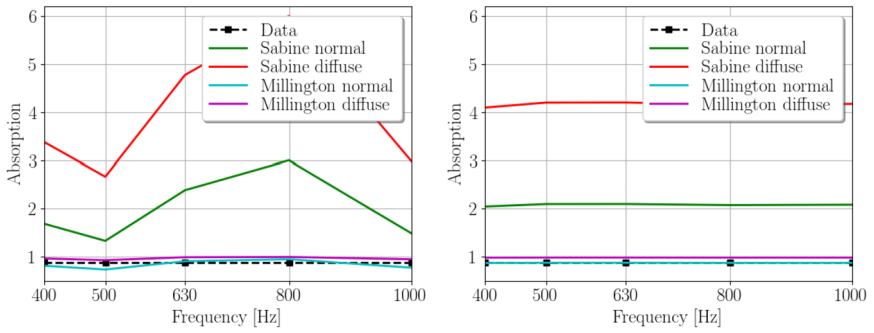

Figure 5 Frequency response of the absorption coefficient associated with a porous sample with surface impedance $Z(\omega) = \beta_s - i\alpha_s/\omega$, where $\alpha_s = 0$ Ns/m^3 and $\beta_s = 206.21$ Ns/m^3, computed by using the Sabine formula (21) and the Millington formula (23), at normal incidence and diffuse field. The absorption coefficients have been obtained using SPL values (left plot) and local L_eq-averages (right plot)

frequency response of the absorption coefficient has been computed from the decay rates (and consequently, from the reverberation times) associated with the SPL values, the local L_{eq}-averages, or the root-mean-square values. Figure 5 shows the frequency response of the absorption coefficient computed at diffuse field and at normal incidence using Sabine's and Millington's formula (see (21) and (23), respectively).

The absorption values are obtained from the SPL time evolution in the left plot, whereas in the right plot, the absorption values are computed from the local L_{eq}-averages. The numerical results are compared with the manufactured data. As observed in both plots of Fig. 5, Sabine's formula overestimates the absorption coefficient, while Millington's formula obtains values closer to the experimental ones. In fact, under normal assumptions, absorption values are predicted accurately by using Millington's formula, with relative errors $\varepsilon_{\text{SPL}} = 10.77\%$ and $\varepsilon_{L_{\text{eq}}} = 1.55\%$. The lowest error obtained with the local L_{eq}-averages confirms the ASTM standard is more robust and less prone to be affected than the algorithms based on the SPL values at concrete time steps. Notice that the absorption coefficient computed assuming a diffuse field is completely erroneous since the current configuration of the piston-like wall generated a normal incident field on the plane where the microphones are located.

4.1.2 Validation test with experimental data

This second two-dimensional simulation considers a material made from polypropylene fibers with thickness $h = 20$ mm. As in the previous manufactured case, where the surface impedance is constant (independent of the frequency), the surface impedance associated with this sample is modelled by $Z(\omega) = \beta_s - i\alpha_s/\omega$, for each angular frequency ω. The surface impedance parameters α and β will be obtained by a least-square fitting problem assuming that the wavenumber and the characteristic impedance of the fibrous material is governed by the classical Miki's model [25], whose physical parameters are the porosity ϕ, the tortuosity α_∞, and the pore shape factor ratio M''. The complex wave number $k(\omega)$, and the characteristic impedance $Z(\omega)$ in the Miki's model are, respectively, given by

$$k(\omega) = \frac{\omega}{c_F}\sqrt{\alpha_\infty}\left(1 + 0.109\left(\frac{\alpha_\infty \omega}{2p\sigma\phi M''^2}\right)^{-0.618} - i0.16\left(\frac{\alpha_\infty \omega}{2p\sigma\phi M''^2}\right)^{-0.618}\right), \tag{24}$$

$$Z(\omega) = \frac{\rho_F c_F}{\phi}\sqrt{\alpha_\infty}\left(1 + 0.07\left(\frac{\alpha_\infty \omega}{2p\sigma\phi M''^2}\right)^{-0.632} - i0.107\left(\frac{\alpha_\infty \omega}{2p\sigma\phi M''^2}\right)^{-0.632}\right), \quad (25)$$

where ρ_F, and c_F are the fluid mass density and sound speed, respectively.

For the present fibrous material, some experimental data measured in a Kundt's tube at normal incidence has been used to set the model parameters, namely, $\phi = 0.83$, $\sigma = 2.29 \times 10^4$ Nm^{-4}s, $\alpha_\infty = 1.02$, and $M'' = 0.95$. Consequently, the surface impedance of a fibrous sample with thickness h at angular frequency ω is given by $Z_s(\omega) = Z(\omega)\coth(ik(\omega)h)$, where $Z(\omega)$ and $k(\omega)$ are the characteristic impedance and the wave number defined in (24) and (25), respectively.

However, the main problem with using the surface impedance with the Miki's model relies on the fact that it cannot be efficiently implemented in a time marching scheme since it involves time convolutional expressions (due to the non-polynomial dependency of Z_s with respect to ω). Hence, the surface impedance associated with Miki's model is considered as ground-truth data, and they are approximated by the simplest model introduced in the time-domain problem (2) to avoid this drawback. With this purpose, the following fitting problem is solved: finding $\alpha_s^* > 0$ and $\beta_s^* > 0$, such as

$$(\alpha_s^*, \beta_s^*) = \underset{\alpha_s>0,\,\beta_s>0}{\arg\min}\left(\frac{\sum_{j=1}^{n} |Z_s(\omega_j) - Z_{anl}(\omega_j, \alpha_s, \beta_s)|^2}{\sum_{j=1}^{n} |Z_s(\omega_j)|^2}\right), \quad (26)$$

where $Z_{anl}(\omega_j, \alpha_s, \beta_s) = \alpha_s + i\omega_j\beta_s$ is the computed surface impedance. The fitting problem (26) has been solved by using a least-square minimization procedure (with a modification of the Levenberg-Marquardt algorithm and where the Jacobian is computed by a forward-difference approximation [27]) with initial guess $(\alpha_s^0, \beta_s^0) = (100, 10)$. The obtained optimal values are $\alpha_s = 6622970.608$ Ns/m^3 and $\beta_s = 293.047$ Ns/m^3, and the relative error in the fitting is $\varepsilon = 1.74\%$. Figure 6 shows the fitting results. The ground-truth data of the absorption coefficient (solid line) and the computed ones with the fitting values α_s and β_s (dashed line) are shown in the left plot. The real and the imaginary parts of the ground-truth values of the surface impedance of the fibrous sample (solid lines) and

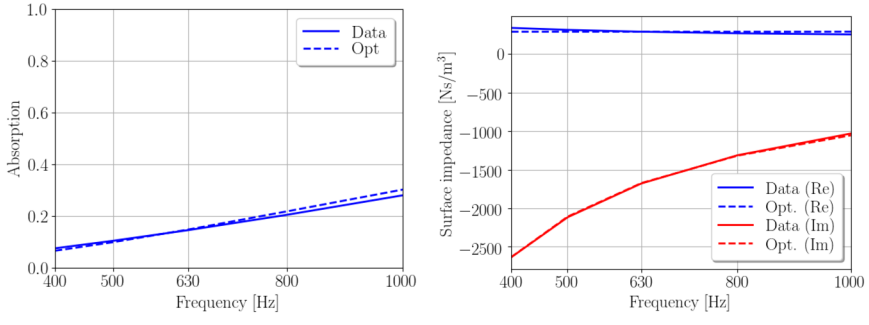

Figure 6 Frequency response of the fibrous sample's absorption coefficient (left) and the surface impedance (right). The solid lines represent the ground-truth values, and the dashed line the fitted values. Real and imaginary parts of both quantities are shown in red and blue lines, respectively

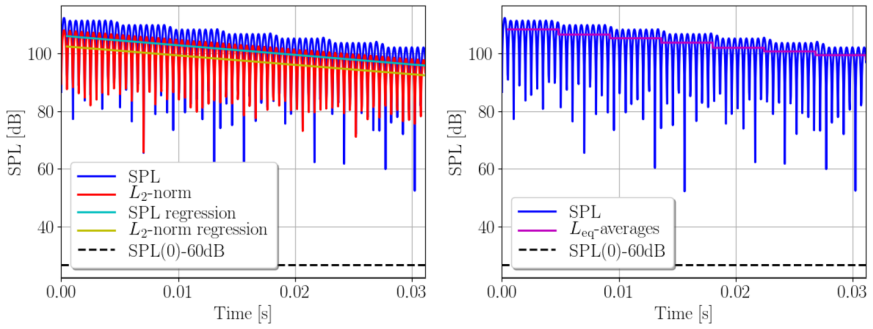

Figure 7 Time evolution of the sound pressure level generated at 1000 Hz for a polypropylene fibrous sample with thickness $h = 20$ mm in a two-dimensional geometry. Left: values of the SPL computed using (18) (blue line), and those obtained by using the L_2-norm of the pressure field (red line), regression line calculated globally by using the SPL data at every time step (cyan line), and regression line computed globally by utilizing the L_2-norm of the pressure field (yellow line). Right: values of the SPL calculated by using (18) (blue line) and regression lines obtained from the local $L_{\mathbf{eq}}$-averages obtained from (19), where the time-window length is $\delta t = 0.00439$ s (magenta line). The dashed black line in both plots represents the SPL value where the initial sound pressure level has decreased by 60 dB

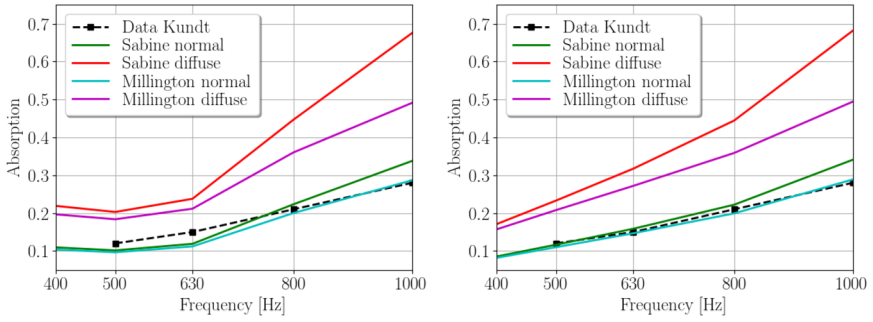

Figure 8 Frequency response of the absorption coefficient associated with a fibrous sample, whose impedance surface is $Z(\omega) = \beta_s - i\alpha_s/\omega$, where $\alpha_s = 6622970.608$ Ns/m^3 and $\beta_s = 293.047$ Ns/m^3. The absorption values have been computed utilizing the SPL values (left plot) and the local $L_{\mathbf{eq}}$-averages (right plot) with normal and diffuse Sabine and Millington's formulas

the computed ones with the fitting values of α_s and β_s are shown in the right plot. In this manner, the values of α_s and β_s obtained with the fitting problem (26) have been used in problems (1) and (2) of the time-harmonic/time-domain hybrid approach.

Once the pressure field is computed at the microphones' locations, the ISO and the ASTM standards can be utilized to estimate the reverberation time at each angular frequency. For this purpose, pointwise SPL values, local $L_{\mathbf{eq}}$-averages, and root-mean-square averages on the entire alpha cabin have been considered. As in the validation test described in Sect. 4.1.1, the frequency ranges from 400 to 1000 Hz in third-octave bands (400, 500, 630, 800, and 1000 Hz).

The decay rates have been computed using a time-domain simulation (2) with a final time $T = 0.030$ s. The ASTM standard has been applied with a time window of length $\delta t = 0.00439$ s. The left plot in Fig. 7 shows that the duration of the simulated time interval is not enough to compute the reverberation time from the SPL values. Hence, a strict application of the ISO standard would increase the required computational time and thereby increase the overall computational cost of the numerical simulation. Figure 8 shows the

absorption coefficient obtained from Sabine's and Millington's formulas (21) and (23), respectively. The absorption values are computed in both plots at normal incidence, i.e., using the typical length $L = V/S$ (see (48)). The numerical results are compared with the experimental data measured in Kundt's tube. In the left plot, the absorption values are computed using SPL values, and in the right plot, the absorption values are obtained by using the local L_{eq}-averages.

As observed in both plots of Fig. 8, at normal incidence, the Sabine formula overestimates the absorption coefficient while the Millington formula predicts the absorption values accurately with relative errors $\varepsilon_{\text{SPL}} = 11.57\%$ and $\varepsilon_{L_{\text{eq}}} = 4.39\%$. This behaviour of the Sabine formula is well-known (in fact, [18] shows that Millington formula gives much more accurate results than Sabine one). Moreover, considering that in a well-designed alpha cabin, the sound field approximates a diffuse field, the absorption coefficients measured in the alpha cabin should be consistent with the values computed in the Kundt's tube [30]. Figure 8 also shows that both Sabine and Millington formulas underestimate the absorption coefficient at diffuse field, although both have the same trend as those computed at normal incidence.

4.2 Three-dimensional simulation

Finally, this section is devoted to the numerical simulation of the absorption coefficient in a realistic three-dimensional alpha cabin. The description of its geometry and the discussion of the numerical results are made using the same fibrous sample utilized in the section above. Figure 9 shows the geometry of the alpha cabin used in this three-dimensional case. This alpha cabin has two non-parallel walls, a volume of 4.5 m^3, and its surface area is approximately 17 m^2.

4.2.1 Geometry

Figure 9 shows the geometry of the alpha cabin used to measure the experimental data.

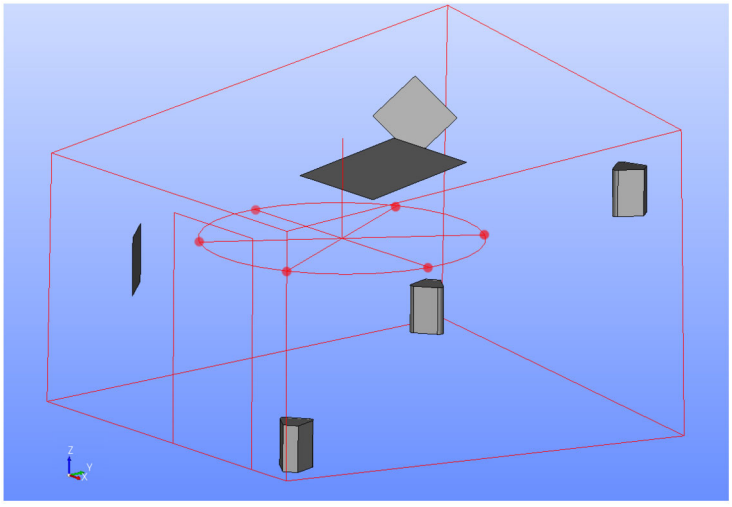

Figure 9 Geometry of the three-dimensional alpha cabin (the edges of the walls are highlighted in red). Plane diffusers and loudspeakers are depicted in grey. The six microphones are located in a circular array marked with red points

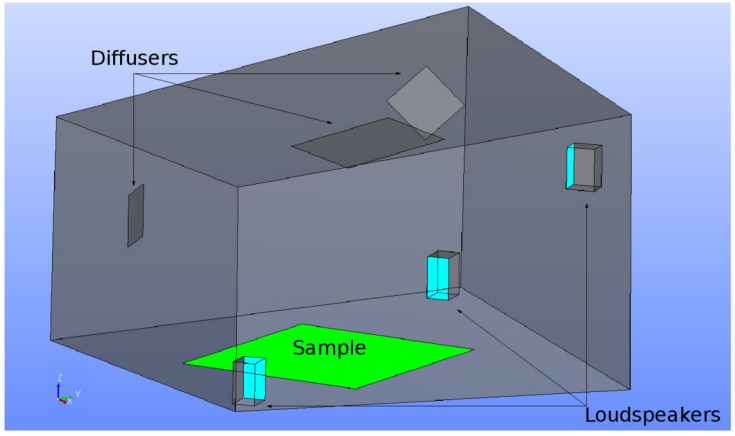

Figure 10 Three-dimensional geometry of the alpha cabin, which includes the rectangular planar diffusers, the rectangular floor location of the porous sample (highlighted in green) and the active faces of the loudspeakers (highlighted in blue)

This alpha cabin is smaller than the standard one recommended in [1], which can not guarantee an adequate generation of a diffusive acoustic field in the time-harmonic problem (1). Even in this case, the proposed time-harmonic/time-domain hybrid methodology can be applied, and it is possible to check if the approximated solution of the time-dependent problem (2) fulfils the diffusivity requirements inside the cabin. There are three loudspeakers, two on the bottom and one on the top of the alpha cabin, six microphones located at the red points shown in Fig. 10, and three rectangular planar diffusers used to achieve a satisfactory diffusion of the field inside the cabin. All the numerical simulations have been performed, taking into account that the fibrous sample has been placed on the floor, neglecting its thickness, and the action of the loudspeakers has been modelled as rigid parallelepipeds where only a planar active face is acting as a piston (see Fig. 10).

The fibrous sample under consideration is identical to that used previously (see Sect. 4.1.2). Following the same fitting procedure, its associated surface impedance is given by $Z_s(\omega) = \beta_s - i\alpha_s/\omega$, with $\alpha_s = 6622970.608$ Ns/m^3 and $\beta_s = 293.047$ Ns/m^3. Again, the reverberation time at each angular frequency has been estimated post-processing different numerical results: the pointwise SPL values, the local L_{eq}-averages, or the root-mean-square averages on the entire alpha cabin. As in the two-dimensional scenarios described in Sect. 4.1, the frequency ranges from 400 to 1000 Hz in third-octave bands (400, 500, 630, 800, and 1000 Hz), as shown in Fig. 11. The decay rates have been computed using the time-domain simulation (2) with a final time $T = 0.20$ s. The ASTM standard has been applied with a time window of length $\delta t = 0.04$ s.

Once the decay rate (or the reverberation time) associated with the SPL values has been calculated, the frequency response of the absorption coefficient can be computed. The left plot in Fig. 12 shows the absorption values calculated using the SPL values while, in the right plot, those obtained with the local L_{eq}-averages can be observed. In both cases, Sabine and Millington's formulas have been applied by using the typical length $L = 4V/S$ (see (22)) of a diffusive acoustic field. The numerical results have been compared with the experimental data measured in Kundt's tube. Even though the experimental data has been measured at normal incidence (as discussed in the two-dimensional numerical

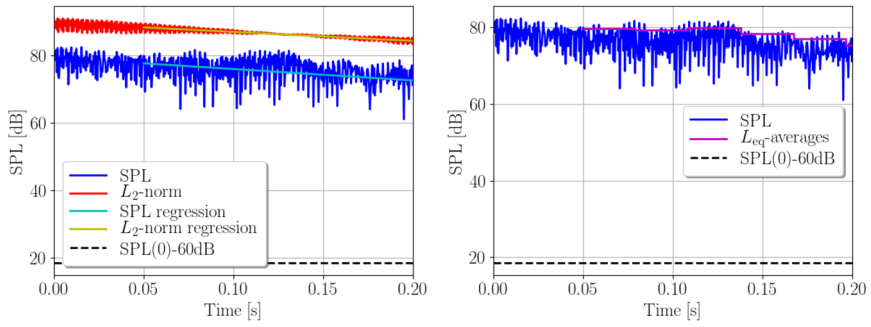

Figure 11 Time evolution of the sound pressure level generated at 1000 Hz for a polypropylene fibrous sample with thickness $h = 20$ mm in a three-dimensional alpha cabin. Left: values of the SPL computed using (18) (blue line), and those obtained by using the L_2-norm of the pressure field (red line), regression line calculated globally by using the SPL data at every time step (cyan line), and regression line computed globally by utilizing the L_2-norm of the pressure field (yellow line). Right: values of the SPL calculated by using (18) (blue line) and regression lines obtained from the local $L_{\mathbf{eq}}$-averages obtained from (19), where the time-window length is $\delta t = 0.0004$ s (magenta line). The dashed black line in both plots represents the SPL value where the initial sound pressure level has decreased by 60 dB

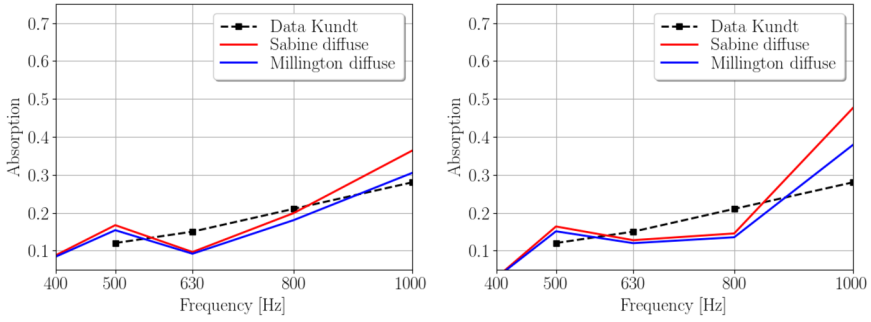

Figure 12 Frequency response of the absorption coefficient associated with a fibrous sample, whose impedance surface is $Z(\omega) = \beta_s - i\alpha_s/\omega$, where $\alpha_s = 6622970.608$ Ns/m^3 and $\beta_s = 293.047$ Ns/m^3 in a three-dimensional alpha cabin The absorption values have been computed utilizing the SPL values (left plot) and the local $L_{\mathbf{eq}}$-averages (right plot) with diffuse Sabine and Millington's formulas

simulations), the frequency response of the absorption coefficient obtained in the three-dimensional case presents a qualitatively similar trend to the experimental absorption data (see [30] for a detailed discussion). Once again, the Millington formula provides more accurate results than the Sabine one, agreeing with the behaviour of the two-dimensional numerical results.

5 Conclusions

This work proposes a time-harmonic/time-domain hybrid procedure to compute the absorption coefficient of a porous sample at diffuse field in an alpha cabin. This methodology is based on the standard ASTM C423-09 [4] to calculate the sound pressure level decay within the alpha cabin. First, a discussion about the models that govern the acoustic alpha cabin behaviour has been shown. Once the mathematical model for the time-harmonic and the time-domain problems have been described in terms of displacement-based variational formulations, they are spatially discretized using first-order Raviart-Thomas finite

elements. The time evolution of the pressure field in the time-domain problem is also discretized in time using a classical implicit Newmark method.

Since the ISO and ASTM standards enforce the use of the time evolution of the SPL values to compute the absorption coefficient in the alpha cabin, different algorithms have been designed to estimate the decay rates and, subsequently, the reverberation time associated with the installation of the porous sample in the cabin. Finally, the absorption coefficient is computed by applying the Sabine or Millington formulas under normal incidence or diffuse assumptions on the generated pressure field.

Some numerical results in two-dimensional and three-dimensional domains have been performed to illustrate the time-harmonic/time-domain hybrid methodology. A two-dimensional test with manufactured data has been used to validate the hybrid procedure. A similar test has also been used to compute the absorption coefficient of a fibrous sample at normal incidence, showing a good agreement between the computed results and the experimental ones obtained in a Kundt's tube. Finally, a realistic three-dimensional alpha cabin has been used to calculate the absorption coefficient, obtaining coherent results with respect to the trend reported in experimental data. Thanks to these numerical experiments, it can be concluded that the proposed hybrid approach represents a numerical tool capable of characterizing porous sample materials at normal incidence or assuming (partial) diffuse fields within the interior of an alpha cabin. In any case, it has been illustrated that the use of local L_{eq}-average (as proposed by the ASTM standard) in combination with Millington's formula is the most robust algorithm among the variety of combinations tested throughout this work.

Author contributions
Conceptualization, A.P. and A.B.; methodology, A.P.; software, L.R.-M. and A.P.; investigation, L.R.-M., A.P., and A.B.; writing original draft preparation, L.R.-M. and A.P.; supervision, A.P. and A.B.; funding acquisition, A.B. and L.R.-M.; All authors read, reviewed, and approved the final manuscript.

Funding information
The first author acknowledges funding from the Spanish Ministry of Universities and the European Union-Next GenerationEU under the project RSU.UDC.MS15. The second author has been supported by MICINN & ERDF project PID2019-108584RB-I00, and also by ED431C 2018/33 - M2NICA (Xunta de Galicia & ERDF). The third author has been supported by MICINN & ERDF project research project MTM2017-86459-R, and also by GI-1563 ED431C 2021/15 (Xunta de Galicia & ERDF).

Data availability
No datasets were generated or analysed during the current study.

Declarations

Competing interests
The authors declare no competing interests.

Author details
[1] Laboratory of Applied Mathematics, DICAM, University of Trento, Via Mesiano 77, 38123, Trento, Italy. [2] CITMAga, Departamento de Matemáticas, Universidade da Coruña, Campus Elviña, 15071, A Coruña, Spain. [3] CITMAga, Departamento de Matemática Aplicada, Universidade de Santiago de Compostela, Campus Vida, 15782, Santiago de Compostela, Spain.

Received: 10 January 2025 Accepted: 28 April 2025 Published online: 15 May 2025

References

1. Ahlersmeyer T. Advanced experimental techniques in vehicle noise and vibration refinement. In: Wang X, editor. Vehicle noise and vibration refinement. Woodhead Publishing; 2010. p. 189–216. https://doi.org/10.1533/9781845698041.2.189.
2. ANSI S1.43. Specifications for Integrating-Averaging Sound Level Meters; 1997. Tech. rep., American National Standard Institute, United States.

3. António J, Godinho L, Tadeu A. Reverberation times obtained using a numerical model versus those given by simplified formulas and measurements. Acta Acust Acust. 2002;88(2):252–61.
4. ASTM C423-09a. Standard test method for sound absorption and sound absorption coefficients by the reverberation room method; 2009. Tech. rep., American Society for Testing Materials, United States.
5. Bathe KJ. Finite element procedures. New York: Prentice Hall; 2008. https://doi.org/10.1002/9780470050118.ecse159.
6. Bécot F, Locqueteau C, Ródenas J. Predicting alpha cabin sound absorption in an industrial context. In: INTER-NOISE and NOISE-CON congress and conference proceedings. vol. 253. Institute of Noise Control Engineering; 2016. p. 4648–58.
7. Bermúdez A, Durán R, Muschietti M, Rodríguez R, Solomín J. Finite element vibration analysis of fluid–solid systems without spurious modes. SIAM J Numer Anal. 1995;32(4):1280–95. https://doi.org/10.1137/0732059.
8. Bermúdez A, Durán R, Rodríguez R, Solomín J. Finite element analysis of a quadratic eigenvalue problem arising in dissipative acoustics. SIAM J Numer Anal. 2001;38(1):267–91. https://doi.org/10.1137/S0036142999360160.
9. Brezzi F, Fortin M. Mixed and hybrid finite element methods. vol. 15. Berlin: Springer; 2012.
10. Carbajo J, Prieto A, Ramis J, Río-Martín L. A non-parametric fluid-equivalent approach for the acoustic characterization of rigid porous materials. Appl Math Model. 2019;76:330–47. https://doi.org/10.1016/j.apm.2019.05.046.
11. Chrisler V. Dependence of sound absorption upon the area and distribution of the absorbent material. J Res Natl Bur Stand. 1934;13(2):169–87.
12. Dance S, Shield B. The complete image-source method for the prediction of sound distribution in non-diffuse enclosed spaces. J Sound Vib. 1997;201(4):473–89. https://doi.org/10.1006/jsvi.1996.0770.
13. Dance S, Shield B. Modelling of sound fields in enclosed spaces with absorbent room surfaces. Part I: performance spaces. Appl Acoust. 1999;58(1):1–18. https://doi.org/10.1016/S0003-682X(98)00064-4.
14. Daniel E. On the dependence of absorption coefficients upon the area of the absorbent material. J Acoust Soc Am. 1963;35(4):571–3. https://doi.org/10.1121/1.1918535.
15. Dragonetti R, Romano R. Errors when assuming locally reacting boundary condition in the estimation of the surface acoustic impedance. Appl Acoust. 2017;115:121–30. https://doi.org/10.1016/j.apacoust.2016.08.024.
16. Duval A, Rondeau J, Dejaeger L, Sgard F, Atalla N. Diffuse field absorption coefficient simulation of porous materials in small reverberant rooms: finite size and diffusivity issues. In: 10ème Congrès Français d'Acoustique. Sociètè Française d'Acoustique; 2010.
17. Hodgson M. On the prediction of sound fields in large empty rooms. J Acoust Soc Am. 1988;84(1):253–61. https://doi.org/10.1121/1.396972.
18. Hodgson M. Experimental evaluation of the accuracy of the Sabine and Eyring theories in the case of non-low surface absorption. J Acoust Soc Am. 1993;94(2):835–40. https://doi.org/10.1121/1.408262.
19. ISO 10534-2:1998. Determination of sound absorption coefficient and impedance in impedance tubes. Part 2: transfer-function method; 1998. Tech. rep., International Standard Organization, Geneva, Switzerland.
20. ISO 354:2003(E). Acoustics - Measurement of sound absorption in a reverberation room; 2003. Tech. rep., International Standard Organization, Geneva, Switzerland.
21. Kehr-Candille V, Ohayon R. Elasto-acoustic damped vibrations. Finite element and modal reduction methods. In: New advances in computational structural mechanics; 1992. p. 321–34. https://hal.science/hal-04114359v1.
22. Kiefling L, Feng G. Fluid-structure finite element vibrational analysis. AIAA J. 1976;14(2):199–203. https://doi.org/10.2514/3.61357.
23. Kuttruff H. Room Acoustics, 5th ed. Spon Press; 2009. https://doi.org/10.3397/1.3455049.
24. London A. The determination of reverberant sound absorption coefficients from acoustic impedance measurements. J Acoust Soc Am. 1950;22(2):263–9. https://doi.org/10.1121/1.1906600.
25. Miki Y. Acoustical properties of porous materials, modifications of Delany-Bazley models. J Acoust Soc Jpn (E). 1990;11:19–24. https://doi.org/10.1250/ast.11.19.
26. Millington G. A modified formula for reverberation. J Acoust Soc Am. 1932;4:69–81. https://doi.org/10.1121/1.1915588.
27. Moré JJ, Sorensen DC, Hillstrom KE, Garbow BS. The MINPACK project. In: Cowell WR, editor. Sources and development of mathematical software. Prentice-Hall, Inc.; 1984. p. 88–111.
28. Nélisse H, Nicolas J. Characterization of a diffuse field in a reverberant room. J Acoust Soc Am. 1997;101(6):3517–24. https://doi.org/10.1121/1.418313.
29. Noh G, Bathe K. An explicit time integration scheme for the analysis of wave propagations. Comput Struct. 2013;129:178–93. https://doi.org/10.1016/j.compstruc.2013.06.007.
30. Olynyk D, Northwood T. Comparison of reverberation room and impedance tube absorption measurements. J Acoust Soc Am. 1964;36(11):2171–4. https://doi.org/10.1121/1.1919339.
31. Raviart P, Thomas J. A mixed finite element method for second order elliptic problems. vol. 606. Berlin: Springer; 1977. p. 292–315. https://doi.org/10.1007/BFb0064470.
32. Sabine W. Collected papers on acoustics. Cambridge: Harvard University Press; 1922.
33. Sakamoto S, Nagatomo H, Ushiyama A, Tachibana H. Calculation of impulse responses and acoustic parameters in a hall by the finite-difference time-domain method. Acoust Sci Technol. 2008;29(4):256–65. https://doi.org/10.1250/ast.29.256.
34. Sandberg G, Ohayon R. Computational aspects of structural acoustics and vibration. CISM International Centre for mechanical sciences. Vienna: Springer; 2009. https://doi.org/10.1007/978-3-211-89651-8.
35. Schroeder M. Measurement of sound diffusion in reverberation chambers. J Acoust Soc Am. 1959;31(11):1407–14. https://doi.org/10.1121/1.1907643.
36. Schultz T. Diffusion in reverberation rooms. J Sound Vib. 1971;16:17–28. https://doi.org/10.1016/0022-460X(71)90392-0.

Publisher's note